Tuning the interlayer spacing of graphene laminate films for efficient pore utilization towards compact capacitive energy storage

Zhuangnan Li[1,2], Srinivas Gadipelli[3,4], Hucheng Li[2,5], Christopher A. Howard[6], Dan J. L. Brett[3], Paul R. Shearing[3], Zhengxiao Guo[1,7,8,9*], Ivan P. Parkin[1*] and Feng Li[2,5*]

Supercapacitors have shown extraordinary promise for miniaturized electronics and electric vehicles, but are usually limited by electrodes with rather low volumetric performance, which is largely due to the inefficient utilization of pores in charge storage. Herein, we design a freestanding graphene laminate film electrode with highly efficient pore utilization for compact capacitive energy storage. The interlayer spacing of this film can be precisely adjusted, which enables a tunable porosity. By systematically tailoring the pore size for the electrolyte ions, pores are utilized optimally and thereby the volumetric capacitance is maximized. Consequently, the fabricated supercapacitor delivers a stack volumetric energy density of 88.1 Wh l^{-1} in an ionic liquid electrolyte, representing a critical breakthrough for optimizing the porosity towards compact energy storage. Moreover, the optimized film electrode is assembled into an ionogel-based, all-solid-state, flexible smart device with multiple optional outputs and superior stability, demonstrating enormous potential as a portable power supply in practical applications.

For the electrochemical energy storage (EES) systems of portable electronics and electric vehicles, the volumetric performance is often a more pertinent figure-of-merit than traditionally used gravimetric performance to assess real-world feasibility[1,2]. Supercapacitors are very promising EES devices for mobile power supplies, since they can deliver high power density, long cycling life and safe operation[3,4]. However, their practical applications are limited by their relatively poor energy density, usually 5–8 Wh l^{-1} in commercialized systems, which is far less than that of batteries (for example, lead–acid batteries typically have an energy density of 50–90 Wh l^{-1})[5–7]. The volumetric energy density (E_{vol}) of a supercapacitor electrode is related to its volumetric capacitance (C_{vol}) and operating voltage window (U), described as:[4,6]

$$E_{vol} = C_{vol} \times U^2/2 \quad (1)$$

Accordingly, E_{vol} can be increased largely by broadening U, which depends substantially on the choice of electrolyte[7,8]. For this reason, organic electrolytes and ionic liquids that permit a wide voltage window (≥3–4 V) are preferred for fabricating high-performance EES devices[8]. On the electrode side, to achieve the highest C_{vol}, both gravimetric capacitance (C_{wt}) and bulk density (ρ) should be simultaneously maximized, due to:[6,9]

$$C_{vol} = C_{wt} \times \rho \quad (2)$$

However, there is typically a trade-off relationship between C_{wt} and ρ. On the one hand, increasing ρ generally reduces porosity and specific surface area (SSA), which are both associated with ion adsorption, and without which C_{wt} drops drastically[2,7,10]. On the other hand, a highly porous material with large SSA is favourable for C_{wt} but often has a low ρ with abundant void spaces, which, when flooded by the electrolyte, substantially increases the weight of the entire device without contributing to the capacitance[1,4,11]. A representative example is the commercially used activated carbons. Although these materials demonstrate considerable C_{wt} (≥200 F g^{-1}), their relatively low ρ (generally ≤0.5 g cm^{-3}) leads to a far from satisfactory C_{vol} below 100 F cm^{-3} (refs. [3,5]). It is clear that enhancing C_{vol} requires materials with structures that balance the density and porosity, rather than merely being highly porous[2,9]. Recently, several strategies for pore engineering have been carried out on graphene-based electrodes to boost C_{vol}[2,6,7,9,10]. For instance, a holey graphene framework was developed through H_2O_2 etching, which facilitated the transport and accessibility of ions in a highly compact form[7]. In another study, a series of graphene monoliths were formed by capillary densification and $ZnCl_2$-assisted annealing, achieving an optimal C_{vol} of 150 F cm^{-3} (ref. [2]). Elsewhere, volatile/non-volatile liquids were used as intercalants to prepare graphene hydrogel films with a high C_{vol} of over 200 F cm^{-3} (ref. [6]). Nevertheless, despite some progress, it is still unclear whether the pores in these systems are storing charge in the most efficient manner, which has become the main obstacle to building better electrodes.

The capacitance contribution per SSA (C_{ssa}) is a valuable metric for evaluating the efficiency of pore utilization for charge storage in an electrode material[12,13]. For example, activated carbons typically exhibit a C_{ssa} of 5–15 μF cm^{-2}, which is lower than for the aforementioned graphene-based electrodes with 20–32 μF cm^{-2} (refs. [5,14]). Interestingly, a recent study measured a breaking of local

[1]Department of Chemistry, University College London, London, UK. [2]Shenyang National Laboratory for Materials Science, Institute of Metal Research, Chinese Academy of Sciences, Shenyang, China. [3]Department of Chemical Engineering, University College London, London, UK. [4]College of Physics, Sichuan University, Chengdu, China. [5]School of Materials Science and Engineering, University of Science and Technology of China, Shenyang, China. [6]Department of Physics & Astronomy, University College London, London, UK. [7]Department of Chemistry, The University of Hong Kong, Hong Kong, China. [8]Department of Mechanical Engineering, The University of Hong Kong, Hong Kong, China. [9]HKU Zhejiang Institute of Research and Innovation, The University of Hong Kong, Hangzhou, China. *e-mail: zxguo@hku.hk; i.p.parkin@ucl.ac.uk; fli@imr.ac.cn

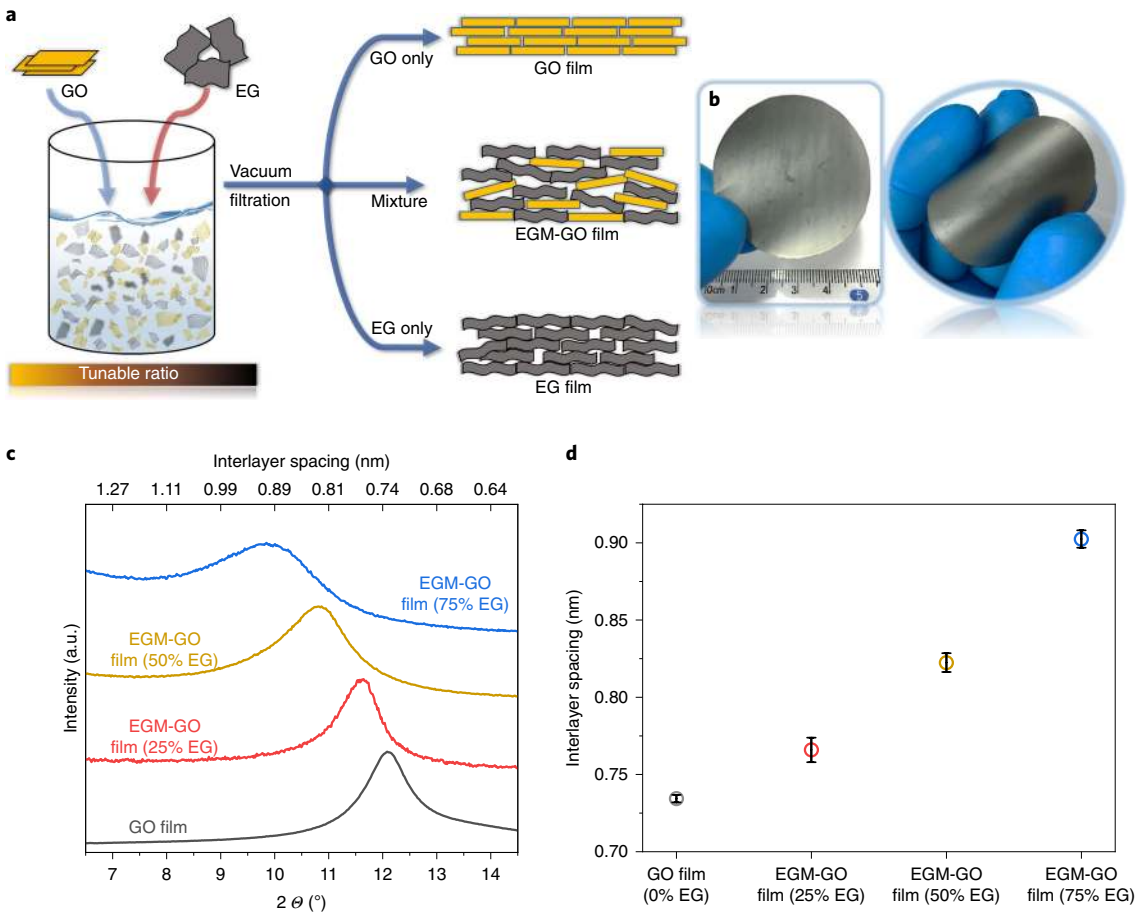

Fig. 1 | Preparation of the EGM-GO films with tunable interlayer spacing. a, Schematic diagram illustrating the production of EGM-GO films from an aqueous dispersion with a tunable precursor ratio of GO to EG. **b**, Photographs of a freestanding EGM-GO film after being peeled off from the filter membrane. **c**,**d**, X-ray diffraction patterns (**c**) and the corresponding *d*-spacing (**d**) of the as-prepared EGM-GO films, showing that the interlayer distance is controllable with the relative weight content of EG. Error bars denote the standard deviations from at least two measurements for three independent samples.

Coulombic ordering when ions are subjected to monolayer confinement[15]. In such a scenario, one can expect that the pores can be more efficiently utilized for charge storage if they can reduce the Coulombic ordering arrangement. Therefore, minimizing the surplus spaces, whilst adapting the pore sizes to that of the electrolyte ions, is a promising strategy to maximize C_{ssa} and thus optimize C_{vol}. However, this strategy requires an electrode material whose pore structure can be precisely controlled. Furthermore, at the scale of a practical EES device, the volume fraction (f_e) of the electrode materials in the whole cell configuration (including both electrodes, current collectors and separator) should also be considered[1,2,6]. A freestanding electrode without binder or conductive additives is more appropriate for maximizing f_e and thereby the E_{vol} of the entire device stack ($E_{vol-stack}$), since:[2]

$$E_{vol-stack} = E_{vol} \times f_e/4 \quad (3)$$

Together, considerations from both the intrinsic features (equations (1) and (2)) and the device perspectives (equations (1) and (3)) provide guidelines for achieving outstanding compact energy storage. Nonetheless, it remains a critical challenge to design an electrode material that is simultaneously freestanding, dense yet porous and applicable to high-voltage electrolytes, while at the same time utilizing its pores efficiently for storing charges.

In this work, we report the design of freestanding graphene laminate films with pores that can be finely tuned by changing the ratio of two precursors, enabling efficient capacitive energy storage. By precisely adapting the pore size to the electrolyte ions, the trade-off between density and porosity is optimized, which allows the film to reach a remarkably high C_{ssa} of 47 μF cm^{-2}. This assembled symmetric supercapacitor can deliver an $E_{vol-stack}$ of 88.1 Wh l^{-1} in an ionic liquid electrolyte, which is superior to peer state-of-the-art carbon-based supercapacitors and even approaches that of lead–acid batteries[6,7]. Moreover, we fabricate an all-solid-state flexible smart device with an ionogel electrolyte, achieving multiple optional outputs (controllable increase of voltage window or capacitance) and thus demonstrating the great promise of this supercapacitor as the power supply for portable electronics.

Preparation and structural characterization

A series of freestanding films was prepared through the vacuum filtration of a graphene oxide (GO) aqueous dispersion containing a controlled amount of exfoliated graphene (EG) (Fig. 1a and Methods). The vacuum-assisted assembly and electrostatic attraction between the sheets facilitated stacking of the GO and EG in a laminated fashion, yielding EG-mediated GO (EGM-GO) films with considerable mechanical flexibility (Fig. 1b and Supplementary Fig. 1). X-ray diffraction patterns of the resultant films revealed information on their average interlayer spacing (Fig. 1c). An intense peak at 12.1° was detected for the pure GO film, corresponding to a *d*-spacing of 0.73 nm. With an increasing EG content, this diffraction peak becomes broader and less intense, gradually shifting to

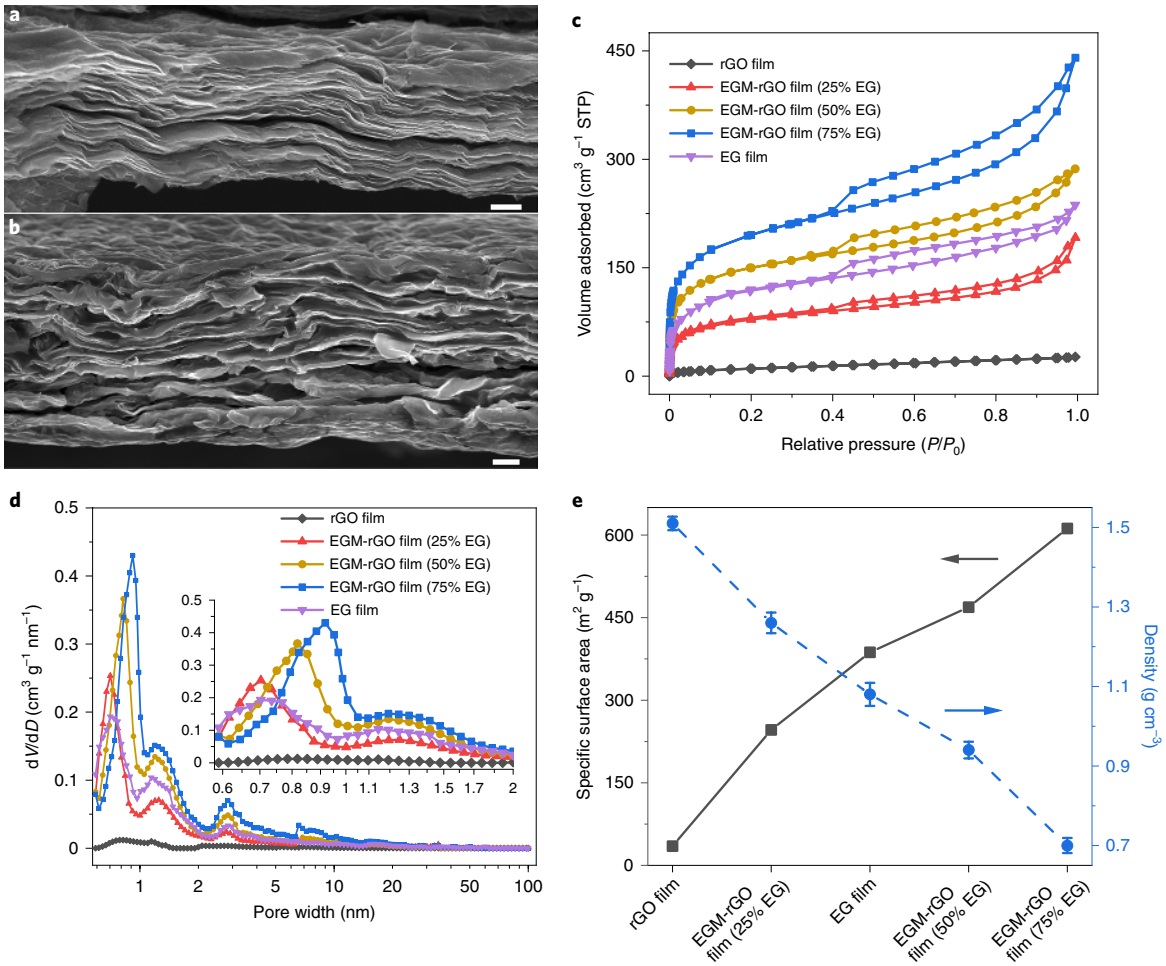

Fig. 2 | Structural characterization of EGM-rGO films. a,**b**, Cross-sectional SEM images of rGO film (**a**) and EGM-rGO (50% EG) film (**b**). Scale bars, 2 µm. **c**,**d**, Ar adsorption–desorption isotherms (STP, standard temperature and pressure) (**c**) and their corresponding pore-size distribution (**d**). The inset in **d** shows a magnified microporous region. **e**, The specific surface area and bulk density of the films demonstrating a trade-off relationship. Error bars denote the standard deviations of density calculation from three independent samples.

a lower angle of 9.8° (*d*-spacing of 0.91 nm). Such an increase in *d*-spacing indicates that the restacking of the GO sheets was disrupted by the coprecipitated EG. The corresponding *d*-spacing of the EGM-GO films is summarized in Fig. 1d, showing that the interlayer distance is incrementally tunable from 0.73 to 0.91 nm by varying the relative EG content from 0 to 75 wt% (Supplementary Figs. 2–4 and Supplementary Note 1). A similar effect was previously demonstrated in the GO laminates, albeit made via a different method, for molecular sieving applications[16].

The as-synthesized films were then subjected to hydroiodic (HI) vapour reduction to enhance their conductivity for use as electrodes. It is worth mentioning that the utilization of HI for reduction is vital, since it can produce a more compact layered architecture on the basis of the nucleophilic substitution reaction mechanism[17]. In comparison, other reduction methods, such as hydrazine treatment or high-temperature annealing, failed to yield a uniform structure. This is because these methods produce CO_2 gas bubbles during the reduction process, leading to superfluous void spaces inside the film (Supplementary Fig. 5). The HI-reduced films exhibited a uniform laminar cross-section as observed in Fig. 2a,b. The reduced GO (rGO) film was flat with sheets densely packed together (Fig. 2a), while in the reduced EGM-GO (EGM-rGO) laminates, the layers were comparatively wrinkled with more interlayer gaps (Fig. 2b). This difference is because the removal of oxygenated functionalities induced restacking of bare rGO sheets through π–π interactions[17]. In contrast, the presence of EG can potentially act as a scaffold to mitigate rGO sheet aggregation, leaving behind slit pores within the EGM-rGO films. Argon adsorption–desorption measurements confirm that the porosity of the EGM-rGO films can be controlled by varying the relative EG content. For instance, the steep uptake at relative pressures (P/P_0) of less than 0.01 in the isotherms indicates that more micropores were created when the proportion of EG increased from 0 to 75 wt% (Fig. 2c). A pure EG film was also prepared for comparison but only showed moderate porosity, inferior to that of EGM-rGO (50% EG). This change stems from the insufficient delamination and dispersion of pure EG in water (without GO acting as a surfactant), which is attributed to the intrinsic hydrophobicity of graphene (Supplementary Fig. 1). All films exhibited a micropore-dominated pore-size distribution (Fig. 2d and Supplementary Fig. 6), demonstrating the effective diminishment of surplus meso- and macropores compared with the precursor (Supplementary Fig. 7). More importantly, for the different films, different sizes of subnanopores were detected across the microporous region (Fig. 2d, inset). For example, prominent pores were ~0.9 nm in width for EGM-rGO (75% EG) but ~0.8 nm for EGM-rGO (50% EG). By changing the fraction of EG, the SSA of the resultant films could be increased from 35 to 612 m^2 g^{-1}; whereas the corresponding bulk density decreased from 1.51 to 0.70 g cm^{-3}

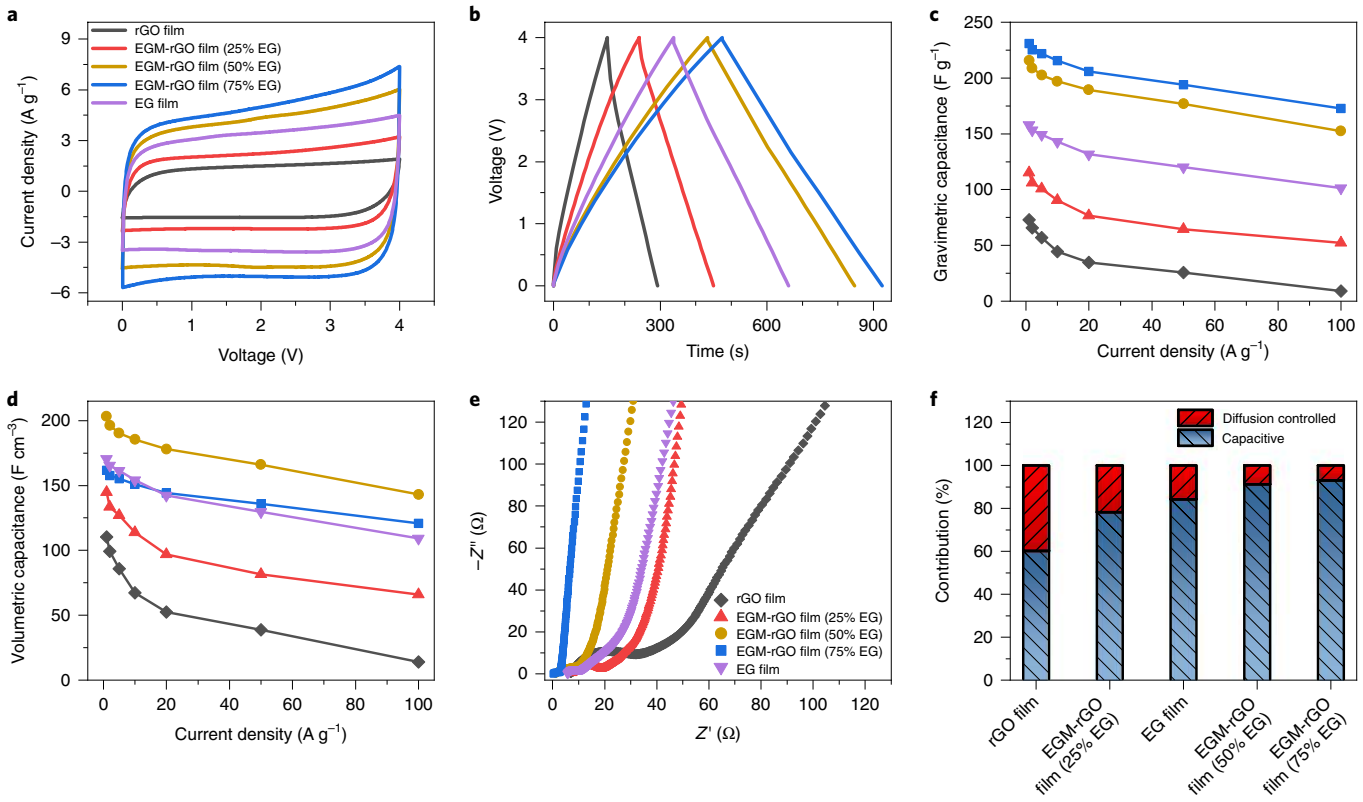

Fig. 3 | Electrochemical characterization of EGM-rGO films-based supercapacitors in $EMIMBF_4$. **a**, CV curves at a scan rate of 50 mV s^{-1}. **b**, GCD curves at a current density of 1 A g^{-1}. **c**,**d**, Gravimetric (**c**) and volumetric (**d**) capacitances versus current densities. **e**, A comparison of the Nyquist plots. **f**, Differentiation of capacitance contribution from CV curves at a scan rate of 10 mV s^{-1}.

(Supplementary Fig. 8), in good accordance with the increasing order of SSA, revealing a typical trade-off relationship as illustrated in Fig. 2e. These results suggested that our approach has enabled freestanding dense films to be produced with controllable porosity, which can then be directly used as electrodes.

Electrochemical characterization of EGM-rGO films

To investigate the electrochemical properties, we fabricated a series of symmetric supercapacitors with neat 1-ethyl-3-methylimidazolium tetrafluoroborate ($EMIMBF_4$) ionic liquid as the electrolyte (Supplementary Fig. 9). It is worth mentioning that, although diluting ionic liquids with organic solvents (such as acetonitrile) can lower their viscosity[8], the as-obtained solvated ions with larger size (>1.30 nm) would be unsuitable for the EGM-rGO electrode with abundant subnanopores (<1 nm) tailored for bare ions (for example, $EMIM^+$ has a diameter of 0.76 nm) (Supplementary Figs. 10 and 11). The cyclic voltammetry (CV) and galvanostatic charge–discharge (GCD) curves exhibited quasi-rectangular and isosceles triangular shapes, respectively, both indicating nearly ideal capacitive behaviour (Fig. 3a,b). Figure 3c summarizes the C_{wt} derived from GCD curves, where EGM-rGO (75% EG) shows the highest value amongst all the films (231 F g^{-1} at 1 A g^{-1}). It is evident that C_{wt} increases concomitantly with the porosity, that is, with the decreasing density. However, the case is very different for C_{vol}, when both C_{wt} and density are simultaneously taken into consideration (equation (2)). As illustrated in Fig. 3d, EGM-rGO (50% EG) yielded the highest C_{vol} of 203 F cm^{-3} at 1 A g^{-1}. Furthermore, the EG film also yielded a higher C_{vol} than EGM-rGO (75% EG) at 1 A g^{-1}, but with the current density reaching 100 A g^{-1}, it retained only 64% of the initial performance while the latter was comparatively stable with more capacitance retention (75%) (Fig. 3d).

To provide further understanding of rate capabilities, we performed electrochemical impedance spectroscopy and capacitance differentiation analyses. Nyquist plots present the responses over a frequency range from 100 kHz to 10 mHz (Fig. 3e). In the low-frequency region, the quasi-vertical curves reveal a nearly ideal capacitive behaviour. In the high-frequency region, a shorter 45° transition line and smaller diameter semicircle indicate a lower charge transfer resistance and more efficient electrolyte diffusion within the electrodes[18]. The ion transport became less efficient with a reduction in porosity of the films. This leads directly to decreased rate capabilities (Fig. 3d), as the electrical double layer only forms along the accessible surface of the pores that ions can penetrate into[3,19]. A representative example is the rGO film ($\rho = 1.51$ g cm^{-3}), which showed a rather poor rate capability (13% retention at 100 A g^{-1}) due to its overly confined interplanar channels between densely packed layers that are unfavourable for ion diffusion. In addition to ion transport, since the rate capability is also closely associated with the charge storage mechanism, capacitance differentiation was carried out. The current responses in the CV curves were separated into capacitive and diffusion-controlled contributions (Supplementary Fig. 12). The capacitive process has faster kinetics at the electrode–electrolyte interface and also relatively higher stability at larger scan rates/current densities compared with the diffusion-controlled process[20]. Thus, a larger proportion of the capacitive process usually enables a better rate capability. Both EGM-rGO (50% EG) and EGM-rGO (75% EG) exhibited a considerable capacitive contribution of over 90% (91% and 93%, respectively) (Fig. 3f), in agreement with their better rate capabilities (70% and 75% retention at 100 A g^{-1}, respectively) amongst all the films. The results suggest that although the dominant pore size (~0.8 nm) of EGM-rGO (50% EG) film is very close to the size of the electrolyte ions (diameter = 0.76 nm for

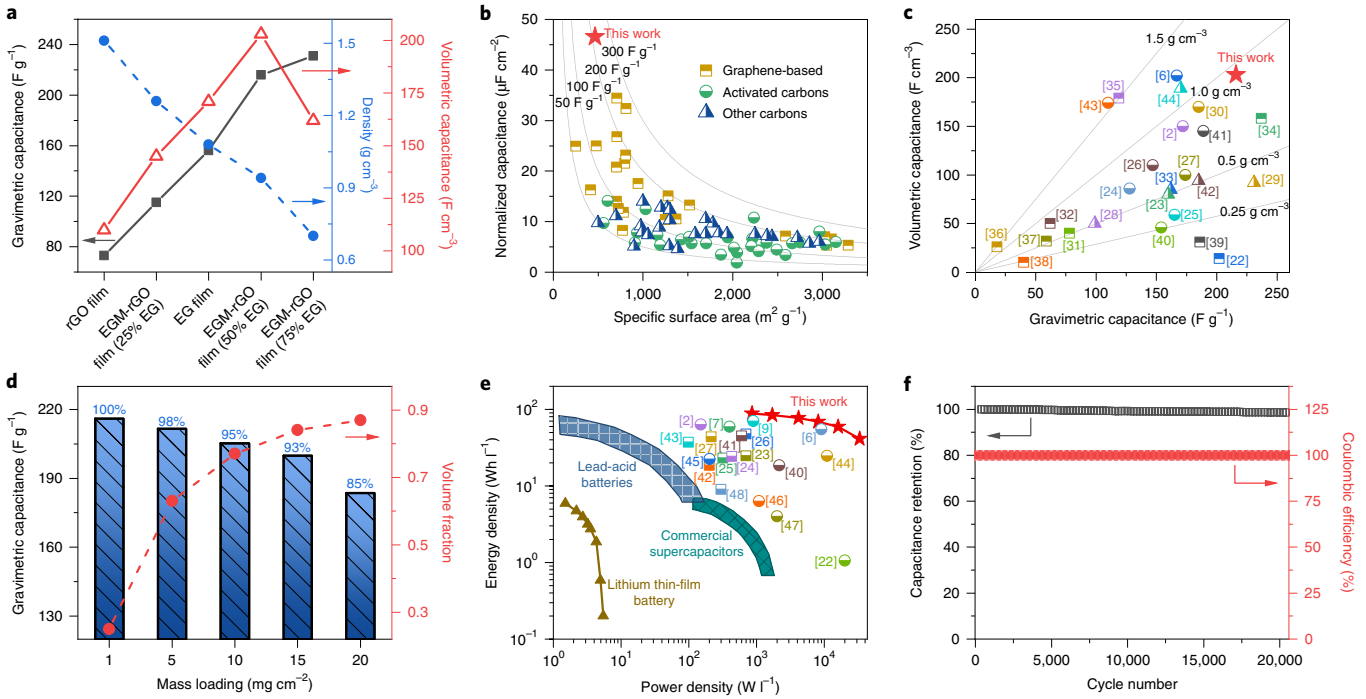

Fig. 4 | Optimizing the device performance towards compact EES. a, Based on the variation in gravimetric capacitance and bulk density of samples, the volumetric capacitance reaches a maximum for the EGM-rGO (50% EG) film. **b**, Capacitance contribution per surface area of EGM-rGO (50% EG) film in comparison with other carbon materials, showing the efficiency of pore utilization in charge storage[2,7,22–33]. Values are collected either from references as such or calculated on the basis of reported capacitance and specific surface area, where the ion-accessible surface area is preferred if applicable. **c**, Gravimetric and volumetric capacitance comparison of EGM-rGO (50% EG) film with reported electrode materials[2,6,22–44]. **d**, Specific capacitance retention with the enhancement of electrode volume fraction (in the whole device) by increasing areal mass loading of the film, which is optimized at 15 mg cm^{-2}. Further increasing mass loading leads to limited enhancement of volume fraction but rapid degradation of specific capacitance. **e**, Ragone plots of EGM-rGO (50% EG) film-based supercapacitor (15 mg cm^{-2} per electrode) in comparison with reported values and state-of-the-art energy storage devices (commercial supercapacitors, lead–acid batteries and lithium thin-film batteries)[2,5–10,22–27,40–48]. Note that all presented energy density and power density values are calculated on the basis of the entire device configuration, rather than the electrode only. **f**, Cycling stability of the device at a current density of 10 A g^{-1}.

EMIM$^+$), the ion transport was not hindered and still remained at high diffusion rates. Such a case is consistent with previous studies, which ascribed this performance to capillary-like forces and surface potential contributions under nanoconfinement[21].

Optimizing the device performance towards compact EES

The optimal electrode for compact EES requires its C_{vol} to be maximized in a wide U electrolyte (equation (1)), where the trade-off relationship between porosity and density needs to be balanced (equation (2)). Figure 4a illustrates this trade-off, showing that C_{wt} can be enhanced with the increased porosity of the films, but alongside a reduction in the bulk density. Initially upon increasing porosity, the C_{wt} increases significantly from 73 to 216 F g^{-1} alongside a density reduction of 38% from 1.51 to 0.94 g cm^{-3}. However, further increasing the porosity merely yields a modest enhancement of C_{wt} but results in a severe loss of bulk density. For example, a C_{wt} increment of only 7% from 216 to 231 F g^{-1} is achieved at the expense of a density drop of 26% from 0.94 to 0.70 g cm^{-3}. Consequently, the C_{vol} is not monotonically enhanced with the increasing porosity, and reaches a maximum value (203 F cm^{-3}) at a bulk density of 0.94 g cm^{-3}. This optimal C_{vol} implies the most efficient charge storage behaviour, which is achieved by EGM-rGO (50% EG) having a C_{ssa} of 47 μF cm^{-2}. Such a C_{ssa} represents a one of the highest efficiency for pore utilization in charge storage for carbon materials, including graphene-based structures, activated carbons, carbon nanotubes, templated carbons and carbide-derived carbons (Fig. 4b and Supplementary Note 2)[2,7,22–33]. The achievement of this remarkable efficiency is ascribed to the abundance of pores in the structure that are optimized with respect to the size of the electrolyte ions. This viewpoint has been further demonstrated by a changing series of electrolytes with different ion sizes (Supplementary Fig. 13 and Supplementary Table 1). Such exceptionally efficient pore utilization thus experimentally supports a recent study where it was suggested that alteration of ion arrangements to a non-Coulombic form can contribute considerably to charge storage (Supplementary Figs. 14–17)[15]. This optimized charge storage also enabled both the C_{vol} and C_{wt} of our EGM-rGO (50% EG) film to simultaneously reach a superior level compared with all carbon-based electrodes tested under comparable conditions (Fig. 4c)[2,6,22–44].

To maximize the $E_{vol-stack}$ at a device level, it is essential to ascertain an optimal f_e of the determined electrode material in the entire supercapacitor configuration (equation (3)). Considering that other components (current collectors and separator) of supercapacitors generally remain unchanged, the f_e can be adjusted by controlling the thickness of the electrodes, or, in other words, the areal mass loading of the material. However, increasing the mass loading is usually accompanied by more sluggish ion diffusion across the thicker electrode, which consequently results in the degradation of both capacitive performance and cycling stability[7]. Hence, the electrode needs to have superior ion transport capability to minimize the influence of incremental mass loading. In this respect, EGM-rGO (50% EG) film exhibited a slight drop in specific capacitance of only 7% as the mass loading increased from 1 to 15 mg cm^{-2} (exceeding the 10 mg cm^{-2} for commercial

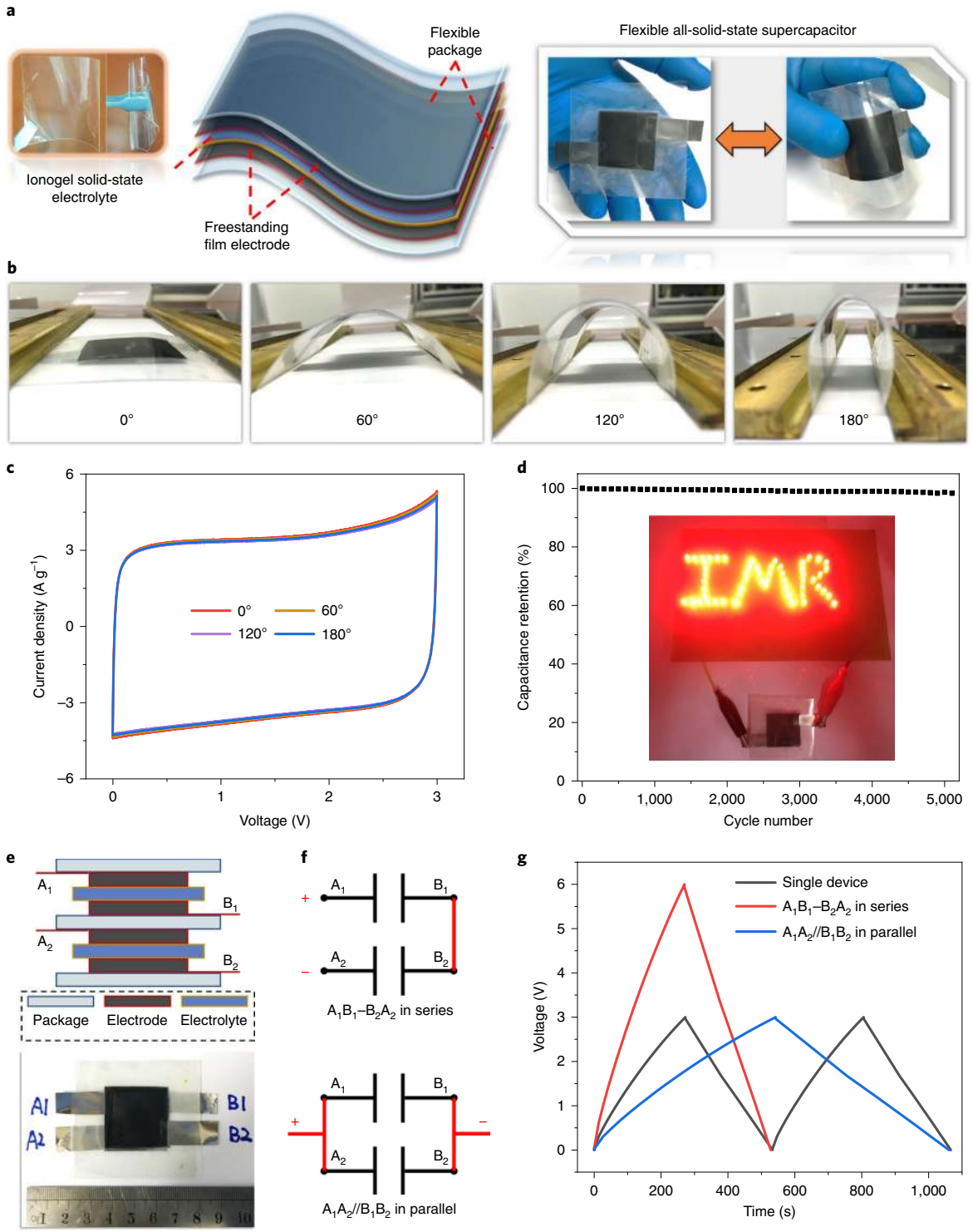

Fig. 5 | Fabrication of ASSC with high-voltage ionogel electrolyte. a, Schematic illustration of the device configuration, with photographs of the solid-state ionogel electrolyte (left) and as-assembled flexible ASSC (right). **b**,**c**, Photographs of the ASSC under various bending angles (**b**) and their corresponding CV curves at a scan rate of 50 mV s^{-1} (**c**). **d**, Cycling stability of ASSC at a current density of 10 A g^{-1}. The inset photograph shows dozens of light-emitting diodes powered by ASSC. **e**, Schematic diagram illustrating the design of a smart ASSC stack, with the photograph of an as-fabricated smart device. **f**,**g**, Circuit diagrams of the connection-dependent outputs by smart ASSC stack (**f**) and their corresponding GCD curves at a current density of 1 mA cm^{-2} (**g**).

carbon-based supercapacitors)[1]. Meanwhile, the f_e improved more than three times from 0.25 to 0.84 (Fig. 4d). Such a high f_e could be attributed to the freestanding nature of the film, which enabled it to be directly used as the electrode without non-active additives (such as binder or conductive agents). Further increasing mass loading over 15 mg cm^{-2} was unfavourable for overall performance (Fig. 4d). Therefore, building on the optimized C_{vol}, U and f_e, the as-fabricated device delivered a $E_{vol-stack}$ of 88.1 Wh l^{-1}, which is one of the highest among state-of-the-art carbon-based symmetric supercapacitors and more than tenfold higher than commercial

supercapacitors (5–8 Wh l^{-1}) (Fig. 4e)[2,5–10,22–27,40–48]. In addition, this $E_{vol-stack}$ even approaches the value for typical lead–acid batteries (50–90 Wh l^{-1}), although with two orders of magnitude higher power density[6,7], highlighting its great potential for practical EES applications. Moreover, our EGM-rGO-based supercapacitor showed excellent cycling stability, with an initial capacitance retention of 98.6% after 20,000 GCD cycles whilst maintaining a Coulombic efficiency of ~100% during cycling (Fig. 4f).

Fabrication of all-solid-state supercapacitor

A wide operating voltage window is the prerequisite for high energy and power densities; however, the widely used aqueous hydrogel polymer electrolytes (≤1 V) in most of the previous studies fall far short of this high-voltage requirement[8,49]. For this reason, we fabricated an EGM-rGO-based all-solid-state supercapacitor (ASSC) using an ionogel electrolyte, $EMIMBF_4$/polyvinylidene fluoride–hexafluoropropylene (PVDF-HFP). Figure 5a schematically illustrates the construction of the ASSC, where the solidified ionogel electrolyte was sandwiched between two symmetric film electrodes and then encapsulated. The as-assembled device (6 cm × 6 cm in dimension) was highly robust and flexible (Fig. 5b). CV curves showed a quasi-rectangular shape and negligible change under various bending angles from 0 to 180° (Fig. 5c), indicating an ideal capacitive behaviour and excellent mechanical stability. A single ASSC was capable of powering dozens of light-emitting diodes with the threshold voltage of ~2 V (Fig. 5d, inset). This device also exhibited an outstanding cycling stability, with 97.8% of the initial capacitance retained after 5,000 cycles at a current density of 10 A g^{-1} (Fig. 5d). Moreover, we developed a smart ASSC stack (Fig. 5e), which can optionally fulfil different output requirements in one device depending on the external connection geometry. For example, by connecting in series or in parallel (Fig. 5f), the smart device achieved a further expanded voltage window (to 6 V from the 3 V for a single ASSC) or boosted capacitance (to 346 mF cm^{-2} from the value of 174 mF cm^{-2} for a single ASSC), respectively (Fig. 5g). Altogether, our ASSC demonstrated several remarkable properties when compared with many previously reported solid-state devices. These merits include a wide operating voltage window, multiple optional outputs (connection dependent), superb mechanical flexibility, high durability and safe operation (avoids leakage of electrolytes, due to non-volatility of the ionic liquid), representing a promising candidate to satisfy the urgent demand for miniaturized electronics.

Conclusions

In summary, our study has demonstrated an approach to maximize the volumetric performance of supercapacitors at a device level by optimizing several important factors (operating voltage, volumetric capacitance and electrode volume fraction). The crucial step is found to be in tailoring the pores of the electrode material for a wide voltage window electrolyte. This is achieved by developing freestanding graphene laminate films with tunable interlayer spacing, which consequently enables the size of slit pores to be precisely adjusted. When pore sizes match the diameter of the electrolyte ions, the film reaches the most efficient pore utilization, and thereby exhibits a well-balanced porosity versus density, leading to an optimized volumetric capacitance. This exceptional efficiency of pore utilization, therefore, experimentally supports the viewpoint that the breaking of ions into a non-Coulombic ordering arrangement in slit pores can contribute considerably to charge storage[15]. With an optimal areal mass loading ascertained subsequently, the symmetric supercapacitor can deliver a stack volumetric energy density of 88.1 Wh l^{-1}. The achievement of such compact energy storage represents a substantial step towards the practical applications for supercapacitors. Furthermore, based on this film, the fabricated, flexible, solid-state smart device with an ionogel electrolyte realizes controllable outputs and excellent durability, suggesting great opportunities for portable power supply in miniaturized electronics and electric vehicles.

Methods

Preparation of EGM-rGO films. Two precursors, GO and EG, were synthesized by an improved Hummers' method and thermal-shock exfoliation, respectively, as described in previous work[44,50]. Briefly, to synthesize GO, graphite powder (1 g) was added to the 9:1 mixture of concentrated H_2SO_4 and H_3PO_4 (22.5 ml:2.5 ml) under vigorous stirring at 0 °C. Next, $KMnO_4$ (6 g) was slowly added to the mixture under persistent stirring at a temperature below 5 °C. The mixture was further cooled to 0 °C and stirring was maintained overnight. The mixture was then slowly heated to 50 °C in an oil bath and left for a day, resulting in a brown paste. Deionized water (120 ml) was slowly added to the paste and stirred for 1 h. Subsequently, H_2O_2 (35%, 9 ml) was added to the solution drop by drop to reduce the unreacted excess $KMnO_4$, and during this process the colour of the solution changed to bright yellow. The solution was stirred for another 1 h and left to settle. Then, the product was washed using dilute HCl (3.5%, 750 ml) to remove the remaining salts, followed by washing with deionized water until neutral. Finally, the GO powder was obtained by freeze-drying.

EG was prepared by inserting a glass tube containing GO powder into a preheated furnace at 400 °C. The thermal shock occurred in less than 2 min after tube insertion. During this process, the bright yellow powder turned to black and became fluffy. Then, the tube was kept in the furnace for another 2 min to ensure completion of the exfoliation process. Finally, EG was collected after the tube had cooled down naturally. The as-reduced EG had an oxygen content of ~13.7 at% with a C:O ratio of 6.3 (Supplementary Fig. 3).

EGM-GO films were prepared by vacuum filtration of the aqueous dispersion of two precursors in a certain mass ratio. Taking the preparation of EGM-GO (50% EG) as an example, GO (12 mg) and EG (12 mg) powders were dispersed in deionized water (120 ml) with the aid of sonication. After centrifugation (2,000 r.p.m. for 10 mins) to leave out the sediment, the homogenous dispersion was then filtered through an anodic aluminium oxide membrane (0.2 μm pore size), followed by air drying and peeling off from the filter. The thickness of the films, that is, the areal mass loading, was adjusted by controlling the dosage of dispersion (concentration remained the same). The reduction of EGM-GO films was carried out by exposing them to HI vapour (a container maintained at 90 °C containing 2 ml of HI acid solution) for 30 mins, during which time the colour of the films changed from matt brown/black to metallic grey. The resultant EGM-rGO films were repeatedly washed with deionized water and ethanol five times to remove any residual HI and then dried at room temperature. As a control, rGO and EG films were prepared with a similar procedure but from pure GO and EG dispersions, respectively. The areal mass loading of all EGM-rGO films was ~1 mg cm^{-2} unless specifically mentioned otherwise.

Structural characterization and analysis. The morphologies of EGM-rGO films were observed with a scanning electron microscope (SEM, FEI Nova NanoSEM 430). The thickness of the films was measured from the cross-sectional SEM images of three independent samples, and the average value used to calculate corresponding bulk density. X-ray diffraction patterns were recorded on a Rigaku diffractometer with CuKα radiation ($\lambda = 1.54184$ Å). Small-angle X-ray scattering was performed using a Ganesha 300XL under vacuum conditions. X-ray photoelectron spectroscopy was investigated with an AlKα source (ThermoFisher Scientific). Fourier-transform infrared spectroscopy measurements were carried out in a transmittance mode with background correction (Alpha FTIR Routine Spectrometer). Ar adsorption–desorption isotherms were collected by Quantachrome Autosorb-iQC at 87 K. Before analysis, samples were outgassed at 180 °C for at least 12 h to ensure minimal intrapore adsorbate. The specific surface area was calculated according to the quenched solid density functional theory (QSDFT), where the ion-accessible surface area was obtained after subtracting the contribution from the pores having a size smaller than the electrolyte ions. The pore size distribution was analysed based on a combination of QSDFT (for micropores and mesopores) and Barrett–Joyner–Halenda (for macropores) methods.

Fabrication of supercapacitors. Supercapacitors were assembled in a symmetric two-electrode configuration to evaluate the electrochemical performance. The working electrodes were prepared by punching the freestanding EGM-rGO film into discs ($\Phi = 16$ mm) and pressing them onto a carbon-coated aluminium foil current collector under 6 MPa. Before the device assembly, as-prepared working electrodes were immersed into pure $EMIMBF_4$ ionic liquid under vacuum overnight to be fully wetted. Fabrication of the supercapacitors was carried out in an argon-filled glovebox. Two working electrodes with a Celgard separator ($\Phi = 19$ mm) in between were assembled into a sandwich-like structure in a CR2032 coin-cell case with neat $EMIMBF_4$ electrolyte.

The ASSC was fabricated with a polyethylene terephthalate (PET) flexible package, EGM-rGO (50% EG) film working electrodes and $EMIMBF_4$/PVDF-HFP ionogel electrolyte. First, PVDF-HFP (0.2 g) was fully dissolved in acetone

(20 ml) by magnetically stirring at 50 °C to yield a clear solution. Then, $EMIMBF_4$ (1.8 g, an optimal mass ratio of $EMIMBF_4$ to PVDF-HFP is ~9) in acetone (5 ml) was added dropwise to the above solution of PVDF-HFP and further stirred for 30 mins. The resultant ionogel electrolyte of $EMIMBF_4$/PVDF-HFP was cast onto the electrode films and left at room temperature for solidification. Finally, two as-prepared electrodes were assembled together to form a working unit, followed by encapsulation with two PET films through a hot-pressing process, where flexible aluminium foils were introduced for outward connection. For fabrication of the smart ASSC stack, a similar procedure was used with alternately assembling PET films and working units, as illustrated in Fig. 5e.

Electrochemical characterization and calculations. All electrochemical measurements were carried out on a Biologic VMP3 workstation at room temperature (25 °C). The maximum voltage window of the supercapacitor was evaluated using a three-electrode configuration, as detailed in Supplementary Fig. 9. The electrochemical impedance spectroscopy tests were conducted at open circuit potential under a sinusoidal signal over a frequency range from 100 kHz to 10 mHz with an amplitude of 10 mV. The cycling stability was recorded during continuous GCD cycles at a current density of 10 A g^{-1}. Quantitative capacitance differentiation was performed on CV curves, using:[20]

$$i(V) = k_1 v + k_2 v^{1/2} \tag{4}$$

where $i(V)$ is the current density response at a fixed potential, k_1 is the capacitive effect factor, k_2 is the diffusion process effect factor and v is the scan rate. Therefore, $k_1 v$ and $k_2 v^{1/2}$ in equation (4) represent the capacitive and diffusion-controlled contribution, respectively.

The gravimetric capacitance of a single working electrode (C_{wt}) was derived from GCD curves, using the following formula:

$$C_{wt} = 2(I \times \Delta t)/(m \times U) \tag{5}$$

where I is the discharging current, Δt is the discharging time, m is the mass loading of the electrode and U is the voltage window after excluding the IR drop. The corresponding volumetric specific capacitance (C_{vol}) was calculated according to equation (2). The volumetric energy density of a single working electrode (E_{vol}) in the device was derived using equation (1). The corresponding volumetric power density (P_{vol}) was obtained from:

$$P_{vol} = E_{vol}/\Delta t \tag{6}$$

The volumetric energy density of the entire device stack ($E_{vol-stack}$) was calculated from equation (3). The corresponding stack volumetric power density was obtained by using the formula:

$$P_{vol-stack} = E_{vol-stack}/\Delta t \tag{7}$$

The volume fraction of electrode materials (f_e) in the entire device configuration was calculated on the basis of the following component thicknesses: ~20 μm for each carbon-coated aluminium foil current collector, ~25 μm for the Celgard membrane separator and ~165 μm for each EGM-rGO (50% EG) film with 15 mg cm^{-2} areal mass landing.

Data availability

All data generated or analysed during the current study are included in this published article (and its Supplementary Information file). Additional datasets related to this study are available from the corresponding author on reasonable request.

References

1. Gogotsi, Y. & Simon, P. True performance metrics in electrochemical energy storage. *Science* **334**, 917–918 (2011).
2. Li, H. et al. Ultra-thick graphene bulk supercapacitor electrodes for compact energy storage. *Energy Environ. Sci.* **9**, 3135–3142 (2016).
3. Simon, P. & Gogotsi, Y. Materials for electrochemical capacitors. *Nat. Mater.* **7**, 845–854 (2008).
4. Wang, Q., Yan, J. & Fan, Z. Carbon materials for high volumetric performance supercapacitors: design, progress, challenges and opportunities. *Energy Environ. Sci.* **9**, 729–762 (2016).
5. Burke, A. R&D considerations for the performance and application of electrochemical capacitors. *Electrochim. Acta* **53**, 1083–1091 (2007).
6. Yang, X., Cheng, C., Wang, Y., Qiu, L. & Li, D. Liquid-mediated dense integration of graphene materials for compact capacitive energy storage. *Science* **341**, 534–537 (2013).
7. Xu, Y. et al. Holey graphene frameworks for highly efficient capacitive energy storage. *Nat. Commun.* **5**, 4554 (2014).
8. Zhong, C. et al. A review of electrolyte materials and compositions for electrochemical supercapacitors. *Chem. Soc. Rev.* **44**, 7484–7539 (2015).
9. Bu, Y. et al. Compressing carbon nanocages by capillarity for optimizing porous structures toward ultrahigh-volumetric-performance supercapacitors. *Adv. Mater.* **29**, 1700470 (2017).
10. Liu, C. et al. Toward superior capacitive energy storage: recent advances in pore engineering for dense electrodes. *Adv. Mater.* **30**, 1705713 (2018).
11. Simon, P. & Gogotsi, Y. Capacitive energy storage in nanostructured carbon-electrolyte systems. *Acc. Chem. Res.* **46**, 1094–1103 (2013).
12. Chmiola, J. et al. Anomalous increase in carbon at pore sizes less than 1 nanometer. *Science* **313**, 1760–1763 (2006).
13. Sheberla, D. et al. Conductive MOF electrodes for stable supercapacitors with high areal capacitance. *Nat. Mater.* **16**, 220–224 (2017).
14. Gu, W. & Yushin, G. Review of nanostructured carbon materials for electrochemical capacitor applications: advantages and limitations of activated carbon, carbide-derived carbon, zeolite-templated carbon, carbon aerogels, carbon nanotubes, onion-like carbon, and graphene. *WIREs Energy Environ.* **3**, 424–473 (2014).
15. Futamura, R. et al. Partial breaking of the coulombic ordering of ionic liquids confined in carbon nanopores. *Nat. Mater.* **16**, 1225–1232 (2017).
16. Abraham, J. et al. Tunable sieving of ions using graphene oxide membranes. *Nat. Nanotechnol.* **12**, 546–550 (2017).
17. Pei, S., Zhao, J., Du, J., Ren, W. & Cheng, H. M. Direct reduction of graphene oxide films into highly conductive and flexible graphene films by hydrohalic acids. *Carbon* **48**, 4466–4474 (2010).
18. Taberna, P. L., Simon, P. & Fauvarque, J. F. Electrochemical characteristics and impedance spectroscopy studies of carbon-carbon supercapacitors. *J. Electrochem. Soc.* **150**, A292–A300 (2003).
19. Salanne, M. et al. Efficient storage mechanisms for building better supercapacitors. *Nat. Energy* **1**, 16070 (2016).
20. Augustyn, V., Simon, P. & Dunn, B. Pseudocapacitive oxide materials for high-rate electrochemical energy storage. *Energy Environ. Sci.* **7**, 1597–1614 (2014).
21. Cheng, C., Jiang, G., Simon, G. P., Liu, J. Z. & Li, D. Low-voltage electrostatic modulation of ion diffusion through layered graphene-based nanoporous membranes. *Nat. Nanotechnol.* **13**, 685–690 (2018).
22. El-Kady, M. F., Strong, V., Dubin, S. & Kaner, R. B. Laser scribing of high-performance and flexible graphene-based electrochemical capacitors. *Science* **335**, 1326–1330 (2012).
23. Izadi-Najafabadi, A. et al. Extracting the full potential of single-walled carbon nanotubes as durable supercapacitor electrodes operable at 4 V with high power and energy density. *Adv. Mater.* **22**, E235–E241 (2010).
24. Wang, X. et al. Efficiently dense hierarchical graphene based aerogel electrode for supercapacitors. *J. Power Sources* **324**, 188–198 (2016).
25. Zhu, Y. et al. Carbon-based supercapacitors produced by activation of graphene. *Science* **332**, 1537–1541 (2011).
26. Murali, S. et al. Volumetric capacitance of compressed activated microwave-expanded graphite oxide (a-MEGO) electrodes. *Nano Energy* **2**, 764–768 (2013).
27. Kim, T., Jung, G., Yoo, S., Suh, K. S. & Ruoff, R. S. Activated graphene-based carbons as supercapacitor electrodes with macro- and mesopores. *ACS Nano* **7**, 6899–6905 (2013).
28. Stoller, M. D., Park, S., Yanwu, Z., An, J. & Ruoff, R. S. Graphene-based ultracapacitors. *Nano Lett.* **8**, 3498–3502 (2008).
29. Zhang, L. et al. Porous 3D graphene-based bulk materials with exceptional high surface area and excellent conductivity for supercapacitors. *Sci. Rep.* **3**, 1408 (2013).
30. Li, H. et al. Compressed porous graphene particles for use as supercapacitor electrodes with excellent volumetric performance. *Nanoscale* **7**, 18459–18463 (2015).
31. Chen, L. F. et al. Flexible all-solid-state high-power supercapacitor fabricated with nitrogen-doped carbon nanofiber electrode material derived from bacterial cellulose. *Energy Environ. Sci.* **6**, 3331–3338 (2013).
32. Wu, Z. S. et al. Three-dimensional nitrogen and boron co-doped graphene for high-performance all-solid-state supercapacitors. *Adv. Mater.* **24**, 5130–5135 (2012).
33. Largeot, C. et al. Relation between the ion size and pore size for an electric double-layer capacitor. *J. Am. Chem. Soc.* **130**, 2730–2731 (2008).
34. Kou, L. et al. Coaxial wet-spun yarn supercapacitors for high-energy density and safe wearable electronics. *Nat. Commun.* **5**, 3754 (2014).
35. Lee, J. A. et al. Ultrafast charge and discharge biscrolled yarn supercapacitors for textiles and microdevices. *Nat. Commun.* **4**, 1970 (2013).
36. Choi, C. et al. Flexible supercapacitor made of carbon nanotube yarn with internal pores. *Adv. Mater.* **26**, 2059–2065 (2014).
37. Chen, X. et al. Novel electric double-layer capacitor with a coaxial fiber structure. *Adv. Mater.* **25**, 6436–6441 (2013).
38. Meng, Y. et al. All-graphene core-sheath microfibers for all-solid-state, stretchable fibriform supercapacitors and wearable electronic textiles. *Adv. Mater.* **25**, 2326–2331 (2013).

39. Xu, Y. et al. Flexible solid-state supercapacitors based on three-dimensional graphene hydrogel films. *ACS Nano* **7**, 4042–4049 (2013).
40. Liu, C., Yu, Z., Neff, D., Zhamu, A. & Jang, B. Z. Graphene-based supercapacitor with an ultrahigh energy density. *Nano Lett.* **10**, 4863–4868 (2010).
41. She, Z., Ghosh, D. & Pope, M. A. Decorating graphene oxide with ionic liquid nanodroplets: an approach leading to energy-dense, high-voltage supercapacitors. *ACS Nano* **11**, 10077–10087 (2017).
42. Huang, H. C., Huang, C. W., Hsieh, C. Te & Teng, H. Electric double layer capacitors of high volumetric energy based on ionic liquids and hierarchical-pore carbon. *J. Mater. Chem. A* **2**, 14963–14972 (2014).
43. Tao, Y. et al. Towards ultrahigh volumetric capacitance: graphene derived highly dense but porous carbons for supercapacitors. *Sci. Rep.* **3**, 2975 (2013).
44. Li, Z. et al. Exceptional supercapacitor performance from optimized oxidation of graphene-oxide. *Energy Storage Mater.* **17**, 12–21 (2019).
45. Chen, Z. et al. High-performance supercapacitors based on hierarchically porous graphite particles. *Adv. Energy Mater.* **1**, 551–556 (2011).
46. Yu, D. et al. Scalable synthesis of hierarchically structured carbon nanotube-graphene fibres for capacitive energy storage. *Nat. Nanotechnol.* **9**, 555–562 (2014).
47. Meng, F. & Ding, Y. Sub-micrometer-thick all-solid-state supercapacitors with high power and energy densities. *Adv. Mater.* **23**, 4098–4102 (2011).
48. Zhong, J. et al. Efficient and scalable synthesis of highly aligned and compact two-dimensional nanosheet films with record performances. *Nat. Commun.* **9**, 3484 (2018).
49. Zhou, F. et al. Electrochemically scalable production of fluorine-modified graphene for flexible and high-energy ionogel-based microsupercapacitors. *J. Am. Chem. Soc.* **140**, 8198–8205 (2018).
50. Gadipelli, S., Lu, Y., Skipper, N. T., Yildirim, T. & Guo, Z. Design of hyperporous graphene networks and their application in solid-amine based carbon capture systems. *J. Mater. Chem. A* **5**, 17833–17840 (2017).

Acknowledgements

This work was supported by the National Science Foundation of China (grant nos. 51525206, 51521091 and 51372253), the Ministry of Science and Technology of China (grant nos. 2016YFA0200100 and 2016YFB0100100), the Strategic Priority Research Programme of Chinese Academy of Science (grant no. XDA22010602), the Key Research Programme of the Chinese Academy of Sciences (grant no. KGZD-EW-T06) and the EPSRC (grant nos. EP/R020973/1, EP/P009050/1, EP/L018330/1, EP/K002252/1 and EP/M009394/1). P.R.S. would like to acknowledge financial support from the Royal Academy of Engineering.

Author contributions

Z.L., S.G. and F.L. conceived and designed the research. Z.L., S.G. and H.L. performed the experiments and the characterization of the materials. Z.L., S.G., C.A.H., I.P.P. and F.L. analysed the data. S.G., C.A.H., D.J.L.B., P.R.S. and Z.G. contributed to the discussion of the results. Z.L., I.P.P. and F.L. wrote the manuscript. All the authors commented on and revised the manuscript.

Competing interests

The authors declare no competing interests.

Additional information